

Deep-Learning Enabled Multicolor Meta-Holography

Dina Ma, Zhancheng Li, Wenwei Liu, Guangzhou Geng, Hua Cheng,* Junjie Li, Jianguo Tian,* and Shuqi Chen*

Multicolor holography, which can store and reconstruct wavefront information of optical waves at multiple wavelength channels, is demonstrated as a powerful platform for colorful image display. Recently, interleaved and segmented metasurfaces have emerged as appealing alternatives to realize the multicolor holography. However, the crosstalk among different wavelength channels can severely lower their performance. How to obtain the nanostructures with on-demand resonance wavelength, bandwidth, and phase delay is the key to overcome this challenge. Here, a hybrid framework composed of a neural network and an evolutionary strategy is proposed to implement the inverse design of nanostructures with desired resonance wavelength, bandwidth, and phase delay. With the proposed hybrid framework, the crosstalk between different wavelength channels can be eliminated by precisely controlling the resonance wavelength and the bandwidth of every nanostructure. As a proof of concept, a multicolor meta-holography for linear polarized light is experimentally and theoretically validated. The proposed hybrid framework provides a powerful platform for the design of metasurfaces for multi-frequency optical manipulation and multiplexing.

have emerged as a versatile platform for the implementation of novel optical functionalities, multi-functional integration, arbitrary wavefront manipulation, and optical multiplexing.^[3–6] The remarkable progresses in metasurfaces in the past decade spurred a revolution of multidimensional optical wavefront manipulation, which amply demonstrated the advantages of metasurfaces for many useful applications, such as optical cloaking,^[7,8] vortex and vector beam generation,^[9,10] optical hologram,^[11,12] and optical focusing.^[13,14] Particularly, metasurface-based holography, named meta-holography, has attracted tremendous interest since it can significantly improve the resolution, quality, diffraction angle, and field of view of the holograms.^[15–20] High-efficient meta-holograms have been well demonstrated in both metallic few-layer metasurfaces and lossless dielectric metasurfaces.^[21–23]


1. Introduction

Metasurfaces are planar arrays composed of subwavelength artificial nanostructures, which have the merits of arbitrary manipulation of the amplitude, polarization, and phase of optical waves.^[1,2] Thanks to their unprecedented capacities for multidimensional manipulation of optical waves, metasurfaces

Multicolor meta-holography, which can store and reconstruct wavefront information of optical waves at multiple wavelength channels, has received a burgeoning amount of interest in recent years since it is invaluable for colorful image display. The critical challenge of multicolor meta-holography is how to realize the independent wavefront manipulation at different wavelength channels. Overall, there are three main approaches: One way is to utilize the k -space frequency multiplexing, in which a single phase profile is used to reconstruct multiple holographic images at all wavelength channels, and the superposition of selected holographic images in different channels at a certain position is realized by off-axis illumination or diffraction.^[24–26] The main disadvantage of this approach is that the unwanted holographic images can be observed in other spatial position. The second method involves polarization multiplexing. The target images at different wavelength channels are stored in different polarization channels.^[27] Therefore, extra polarization analyzer is essential for the reconstruction of the colorful holographic images. The last and the widely used approach is utilizing the super unit cell composed of several nanostructures with wavelength-dependent resonances to store different wavefront information.^[28–32] Although the enlarged period of the unit cell slightly reduces the quality of the hologram, this approach is still desirable since it is concise and easy to implement than the other two methods. To realize the multicolor meta-holography with a high quality, the crosstalk between different wavelength channels should be eliminated. Therefore, how to obtain the nanostructures with on-demand resonance wavelength, bandwidth,

D. Ma, Z. Li, W. Liu, G. Geng, H. Cheng, J. Tian, S. Chen
The Key Laboratory of Weak Light Nonlinear Photonics
Ministry of Education
Renewable Energy Conversion and Storage Center
School of Physics and TEDA Institute of Applied Physics
Nankai University
Tianjin 300071, China
E-mail: hcheng@nankai.edu.cn; jjtian@nankai.edu.cn;
schen@nankai.edu.cn

J. Li
Beijing National Laboratory for Condensed Matter Physics
Institute of Physics
Chinese Academy of Sciences
Beijing 100190, China
S. Chen
The Collaborative Innovation Center of Extreme Optics
Shanxi University
Taiyuan, Shanxi 030006, China

 The ORCID identification number(s) for the author(s) of this article can be found under <https://doi.org/10.1002/adom.202102628>.

DOI: 10.1002/adom.202102628

and phase delay is a critical question. However, the primary mean for the optimization of nanostructures is an iterative process of trial and error based on numerical simulation, which is time consuming and inefficient for such a multi-objective optimization target.

Recently, deep-learning (DL) has attracted much attention in nanophotonics since it can realize the quick design of nanostructures with desired optical responses and is efficient for multi-objective optimization problem.^[33] The remarkable capabilities of DL have been well demonstrated in domains including computer vision,^[34] speech recognition,^[35] and decision making.^[36] Its superior performance comes from its ability to automatically extract features from large amounts of data layer by layer and discover the intricate, nonintuitive relations between the data. DL has been used to accurately predict optical resonance spectrum and perform inverse optimization of photonic nanostructure.^[37–41] The computational speed of DL is several times faster than conventional numerical simulation, thus greatly improving the speed of optimization procedure. Hence, DL is an appealing alternative to realize the inverse design of nanostructures with on-demand resonance wavelength, bandwidth, and phase delay, which enable colorful meta-holography with low crosstalk and high efficiency.

Here, we demonstrate the use of a DL framework for the inverse design of dielectric nanostructures with on-demanded resonance wavelengths, bandwidths, and phase delays, and the realization of the multicolor meta-holography. The hybrid framework consists of a deep neural network (DNN) and an evolution strategy (ES) algorithm. The DNN is trained to directly connect the structural parameters of nanostructures to their complete optical responses, while the ES algorithm is used to retrieve the structural parameters of nanostructures for the given optical responses. Our inverse design method can produce suitable structural parameters of nanostructures to fulfill the requirements, such as operating wavelength, resonance bandwidth, resonance phase, etc. The proposed hybrid framework is a promising candidate for automatic, rapid design of optical multiplexing metasurfaces with multiple wavelength channels.

2. Results and Discussion

Figure 1a shows the artistic rendering of the inversely designed all-dielectric metasurfaces for multicolor meta-holography. In order to improve the degrees of design freedom of nanostructures and eliminate the crosstalk between different wavelength channels, the unit cells in the designed metasurface are composed of two kinds of anisotropic dielectric nanostructures that can manipulate the amplitude and phase of optical waves at a certain operation waveband at the subwavelength scale. The designed holographic image contains an image of flower of red, green, and blue colors, which can be reconstructed with low crosstalk under the x -polarized white light illumination composed of 470, 550, and 610 nm laser beams. As shown in Figure 1b,c, the two kinds of anisotropic dielectric nanostructures are Titanium dioxide (TiO_2) nanorods and dimers. The structural parameters of nanorods are described by a parameter array $\mathbf{D}_{\text{rod}} = [p_x, p_y, h, l, w]$, while the structural parameters of the dimer structures are described by the other parameter array $\mathbf{D}_{\text{dimer}} = [p_x, p_y, h, l_1, l_2, l_3, l_4, w_1, w_2]$.

In order to train the DNN to predict the optical responses of these two kinds nanostructures, 17 600 samples of nanorods and 17 000 samples of dimer nanostructures were built based on the numerical simulation. Every sample contains the structural parameters of the nanostructure represented by the corresponding parameter array and its reflection coefficient \mathbf{S}_{xx} composed of both the real part (\mathbf{S}_{real}) and imaginary part (\mathbf{S}_{imag}) with a dimension of 1×201 . The reflection coefficient \mathbf{S}_{xx} was obtained by numerical simulation over a wavelength span from 400 to 800 nm that covers the visible spectral range. For the purpose of improving the fitting effect, the Principal Component Analysis (PCA) method was used in the proposed hybrid framework to reduce the dimension of \mathbf{S}_{real} and \mathbf{S}_{imag} . First, the dimensions of the two matrices \mathbf{S}_{real} and \mathbf{S}_{imag} are changed to 1×500 by interpolation. The two matrices are then transformed into low-dimensional feature arrays \mathbf{f}_{real} and \mathbf{f}_{imag} based on PCA method. For the two kinds of nanostructures, there are two independent neural networks to train \mathbf{f}_{real} and \mathbf{f}_{imag} respectively. Figure 1d shows the architecture of the DNN model, which

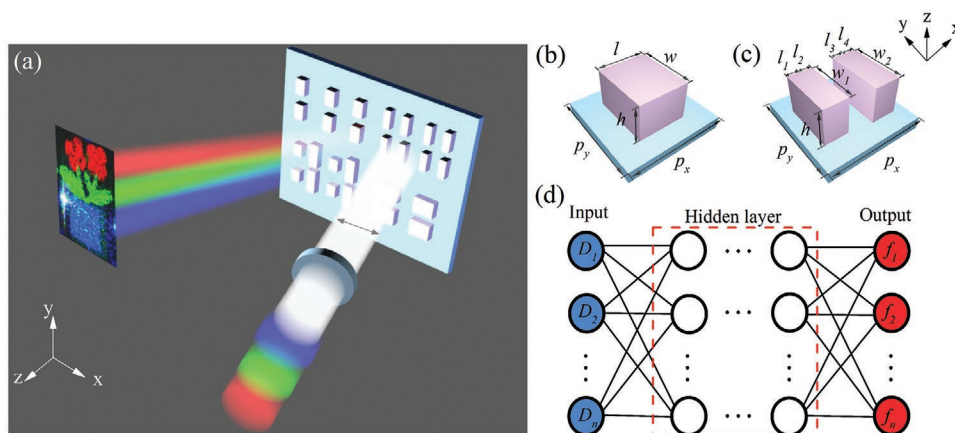


Figure 1. a) An artistic rendering of the inversely designed all-dielectric metasurfaces for multicolor meta-holography, which can be reconstructed under the x -polarized white light illumination composed of 470, 550, and 610 nm laser beams. Two kinds of anisotropic dielectric nanostructures that make up the metasurface: b) the nanorod and c) the dimer. d) The architecture of DNN that takes device designs and PCA features as inputs and outputs respectively.

is a fully connected network with four hidden layers. Every hidden layer contains 500 neurons, and every layer between the input layer and the last hidden layer is preceded by a rectified linear unit (ReLU) activation function. To further expound the training process of the DNN, we take the DNN for the prediction of the f_{real} of the nanorod as an example. The input of DNN was a 16×5 geometric parameter matrix, and the output was a matrix with size 16×50 , where 16 is the number of the batchsize. We used 85% of the simulated data for training and the remaining 15% for testing. The mean absolute error (MAE) is used to represent the loss function between the network's output and f_{real} , and the specific form is $\text{Loss} = \frac{1}{m} \sum_{i=1}^m \left| \text{output}_i - \frac{f_{\text{real}_i}}{2} \right|$.

The weight parameters of DNN are trained using an Adaptive Moment Estimation (Adam) optimizer, and the weight delay is set to be 10^{-5} . The initial learning rate is 10^{-4} , and is lowered by ten times at epoch 300. After 400 epochs, the training of the network is completed, and the loss function values of the corresponding training dataset and test dataset are stable at 0.028 and 0.040, respectively. The architectures of the other three networks are the same as the one shown in Figure 1d, which were trained with the same process. All the DNN were trained by using a computer with a single 6GB GPU (GTX 1660 Ti), and the training process of each network takes 30 min. The hyperparameters and learning curves of all networks can be founded in Table S1 and Figure S1 (Supporting Information).

To validate the performance of the well-trained DNN, we randomly selected two sets of data from the test sets of the two structures to evaluate the prediction accuracy of the DNNs. The predicted results of S_{real} , S_{imag} , the square of the amplitude (S), and the phase (P) of S_{xx} for a nanorod are shown in Figure 2a–d respectively, while those of a dimer nanostructure are shown in

Figure 2e–h. The square of the amplitude (S) and phase (P) of S_{xx} can be expressed as:

$$S = S_{\text{real}}^2 + S_{\text{imag}}^2 \quad (1)$$

$$P = \tan^{-1} \frac{S_{\text{imag}}}{S_{\text{real}}} \quad (2)$$

The predicted results in Figure 2 are in good agreement with the simulated ones. The errors between the predicted and the simulated results at some frequencies can be mainly attributed to the information loss during the process of matrix dimension reduction since the spectra reconstructed by PCA method cannot perfectly fit the initial simulation results (see Figure S2, Supporting Information). At the meantime, there are errors between the prediction features and the real PCA features, which is also contributed to the errors between the final reconstructed spectra and the actual simulated result. For the test dataset of nanorod, the MAE losses between the predicted and simulated results of S_{real} , S_{imag} , S , and P are 0.0197, 0.0195, 0.0173, and 0.129 rad, respectively, while those for the test dataset of dimer are 0.0204, 0.0209, 0.0149, and 0.180 rad, which validates that the DNNs can achieve high-precision prediction for most of the test data and replace the time-consuming numerical simulation process to achieve fast prediction of the amplitude and phase values of x -polarized reflection waves for the two kinds nanostructures.

We further design an ES algorithm to realize the inverse design of nanostructures with on-demand resonance wavelength, bandwidth, and phase delay. The advantages of ES algorithm over other deep-learning inverse design methods based on gradient descent method is that it doesn't relies on the gradient information and is helpful for complex optimization

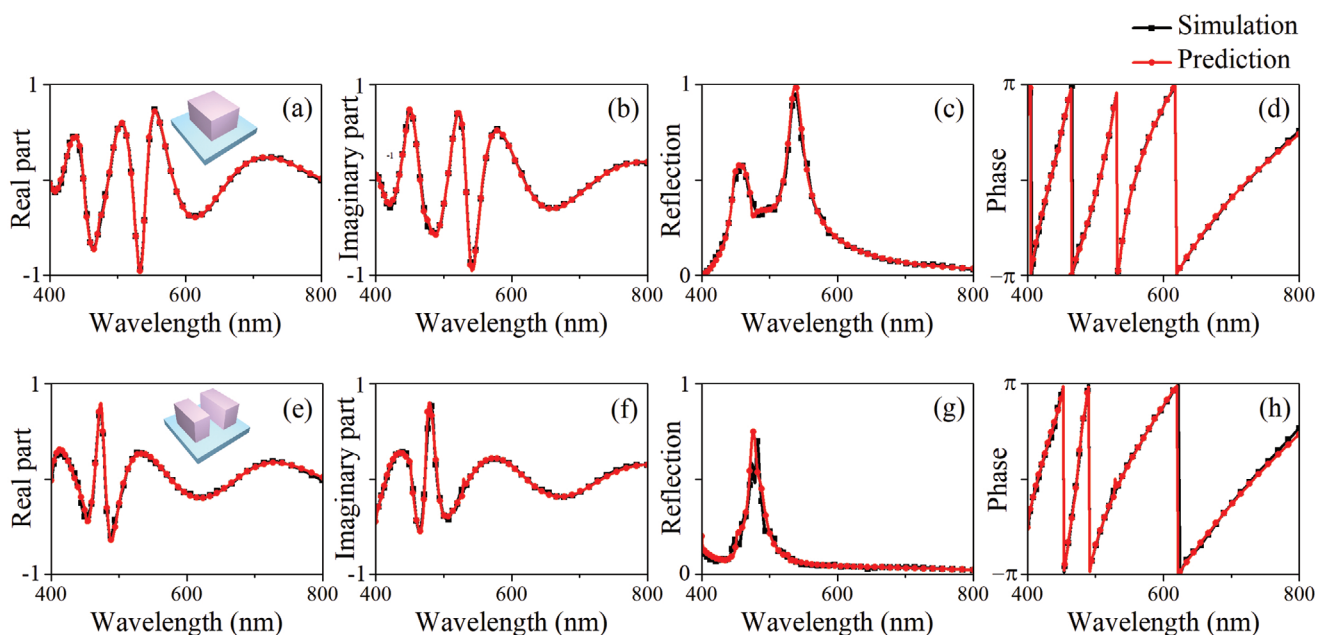


Figure 2. The quantitative analysis on the performance of the well-trained DNNs. a–d) The predicted (red dot line) and the simulated (black dot line) results of S_{real} , S_{imag} , S , and P of a nanorod structure. e–h) The predicted (red dot line) and the simulated (black dot line) results of S_{real} , S_{imag} , S , and P of a dimer structure.

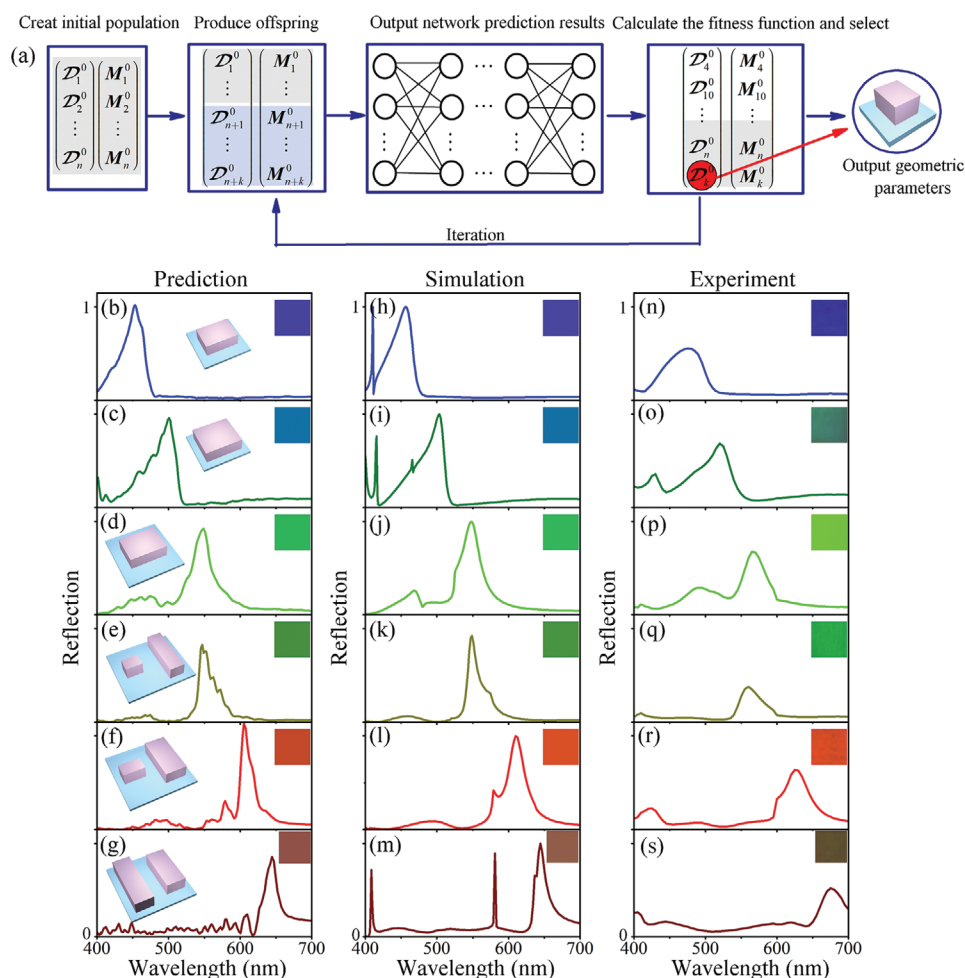


Figure 3. a) Schematic of the modules of the hybrid framework. In each iteration, populations undergo recombination and mutation to produce offspring. The ES algorithm uses matrix operation to calculate the scores of all individuals in the population, and then select the best individuals to move on to the next round of evolution. Panels (b) to (g) are predicted reflection spectra of nanostructures designed by ES algorithm. Panels (h) to (m) are simulated reflection spectra of nanostructures designed by ES algorithm. Panels (n) to (s) are experimental reflection spectra of nanostructures designed by ES algorithm. The parameters of all structures in this figure can be found in Table S2 (Supporting Information).

problems. ES algorithm is a numerical optimization algorithm which imitates the survival process of biological evolution. The process of EM can be described as: a large initial population as the parent is generated first, then some individuals in the initial population are recombined and mutated to produce a certain number of offspring. The offspring and initial population will form a new population. After that, the fitness function values of all the individuals in the population are calculated. The individuals with good scores can continue to enter the next round of evolution, and the individuals with poor scores will be eliminated. In the end, the whole population will evolve in the on-demand direction. To realize the inverse design of the two-kinds of nanostructures, we implement the ES method based on DNN in the form of matrix operation, which can complete hundreds of data calculations in a few seconds, greatly reducing the time cost of inverse design, and also provide convenience for the optimization of various complex problems. As shown in Figure 3a, the initial population in the ES algorithm for the inverse design of nanorod is a matrix with dimension of 500×5 (for the inverse design of dimer nanostructure, the dimension

is 500×9). The rows of the matrix represent the individuals in the population. The dimension of the mutation matrix is in consistent with the that of the population matrix. Every row in the mutation matrix can be expressed as a 1×5 array M , where $M = [M_p, M_p, M_h, M_l, M_w]$. Each element of M is a random number with standard normal distribution, which can realize the random evolution of structural parameters. Two rows of the population matrix are randomly selected, and the elements in the two rows are randomly exchanged (the mutation matrix is also exchanged in the same way) to generate an offspring in the recombination process. The offspring contains the information of two parent individuals, and then it needs to mutate according to the mutation factor. The formula can be expressed as:

$$M_i^j = \max(M_i^j - a - 0.8, 0) \quad (3)$$

$$D_i^j = D_i^j + bM_i^j \quad (4)$$

where a and b are random numbers following a standard normal distribution. By repeating the above-mentioned pro-

cess, we get an offspring with 200 individuals and the dimension of the population matrix is 700×5 . Then, we input the population matrix into the DNN, and obtain the amplitude and phase spectra of the reflection waves. The predicted results are two 700×201 matrices. Each row of the two matrices is the predicted arrays of the amplitude and phase spectra for the reflection waves corresponding to the parameter array of the population matrix. The resonance wavelength and bandwidth are inversely designed by fitting a Gaussian-like spectral line that can be expressed as:

$$g(x) = \frac{1}{\sigma\sqrt{2\pi}} e^{-\frac{(x-\mu)^2}{2\sigma^2}} \quad (5)$$

where μ and σ control resonance wavelength and bandwidth respectively. The fitness function is:

$$F(\mathbf{S}, \mathbf{g}) = -\frac{1}{m} \sum_{i=1}^m (S_i - g_i)^2 \quad (6)$$

where m is the number of elements in \mathbf{S} . S_i and g_i are the i element in \mathbf{S} and \mathbf{g} . We rank the population matrix according to the value of the fitness function from the lowest to the highest by calculating the fitness function. The last 500 rows in the matrix are taken as the population for the next evolution after sorting. After 50 iterations, we can get the optimal geometric parameters, which only takes a few seconds. Specially, we can limit the range of structural parameters of the population according to the fabrication accuracy. For example, in order to achieve one-step fabrication, we can fix the value of h and optimize the remaining parameters.

To show the performance of the proposed hybrid framework, we set three Gaussian-like target spectra for the inverse design of the nanorods with resonance wavelengths of 450, 500, and 550 nm, respectively, whose bandwidths are about 35 nm. Meanwhile, for the inverse design of the dimer structures, the resonance wavelengths of the three Gaussian-like target spectra are 550, 600, 650 nm, and the bandwidths are also 35 nm. Figure 3b–s shows the predicted, simulated, and experimental results of the reflection spectra of the inversely designed nanorods and dimer structures. The reflection spectra of the inversely designed samples were measured by using a home-built optical setup, see Figure S3 (Supporting Information). The results in Figure 3b–g indicate that the resonance wavelength and bandwidth of the reflection spectra of the inversely designed nanostructures are in consistent with the design targets. The experimental results are in reasonable agreement with the predicted and simulated results, which further validate the efficiency of the inverse design method. Although the resonance wavelength in the experimental results show a red shift and the reflection efficiency decreases, the reflection spectra of the fabricated samples are close to our expectations and display the designed color. The differences between the simulated and experimental results are due to the following reasons: First, the red shift of the resonance wavelength is attributed to that the fabricated nanostructures are little larger than the designed ones. Meanwhile, the decrease of the reflection efficiency is due to the rough top surface of the TiO_2 nanostructure that is caused by an inadequate exposure dose of the electron beam lithography. Note that the simulated results were obtained

under normal illumination while the experimental results were measured over a finite incident angle, which also causes the differences between the simulated and experimental results. In order to verify the bandwidth control effect of our method, we further compared the inverse design results under different fitness functions and bandwidths (Figure S4, Supporting Information). The results validate that our method can obtain the most ideal structural parameters according to different target bandwidths. Meanwhile, we can effectively improve the reflectance at the target wavelength by changing the fitness function, which is quite beneficial for the designing of high-efficiency structural color devices.

Importantly, our method is effective for multitask optimization. To make a proof of concept, we designed phase modulated nanostructures at 470, 550, and 610 nm to reconstruct a multicolor holographic image. In the inverse design process, the bandwidth (25 nm) and resonance wavelengths (470, 550, and 610 nm) of the spectra are still designed by giving a Gaussian-like spectral line. In order to simultaneously modulate the resonant wavelength, bandwidth and phase, the fitness function needs to be changed:

$$F(\mathbf{S}, \mathbf{g}) = \left(-\frac{1}{m} \sum_{i=1}^m |S_i - g_i| \right) - \frac{1}{5} |p_{\text{Pre}} - p_{\text{Target}}| - \frac{1}{3} |r_{\text{Pre}} - r_{\text{Target}}| \quad (7)$$

where $P_{\text{Pre}}/P_{\text{Target}}$ and $r_{\text{Pre}}/r_{\text{Target}}$ are the predicted/target phase and reflection values at the target wavelength. Four basic nanostructures with different phase delay effect are inversely designed for every wavelength. The phase modulated nanostructures are designed with a fixed height and limited value range of period with the consideration of the manufacturability of the metasurface. The period in both the x and y directions of every nanostructure is restricted to a common divisor of the pixel size (6 μm) of the designed metasurface, while the height of all nanostructures is fixed at 300 nm to realize a high reflectance. As shown in Figure 4, the reflectance of most inversely designed nanostructures at the resonance wavelengths are close to 100%, while their operation bandwidths are narrow that results in the elimination of the crosstalk between the three designed wavelengths. We used the inversely designed nanostructures to realize the multicolor meta-holography. The information of a multicolor holographic image was stored in a designed metasurface composed of the two kinds of nanostructures (12 basic structures) by using Gerchberg–Saxton (GS) algorithm, as shown in Figure 5a. We get the phase distribution of the three channels first, then we integrate the three independent phase distributions together to get the final phase profile. Specially, since the size of the holographic image is related to the wavelength of the optical waves, the colorful images is scaled correspondingly in the process of hologram design. The scaling factor k_λ of the three channels should satisfy the following relationship: $\lambda_1 k_{\lambda_1} = \lambda_2 k_{\lambda_2} = \lambda_3 k_{\lambda_3}$. More details of the designed phase distribution can be found in Figure S5 (Supporting Information). It is important to note that, since the value range of the nanostructure height and period are limited in the inverse design process, the four phases selected at each wavelength do not cover the entire 2π phase space, as shown in Figure 4g–l. For example, it is difficult to obtain a nanostructure in which the phase delay equals to 180° at 470 nm, or 108° at 550 nm, or -108° at 610 nm. Therefore, we used a modified

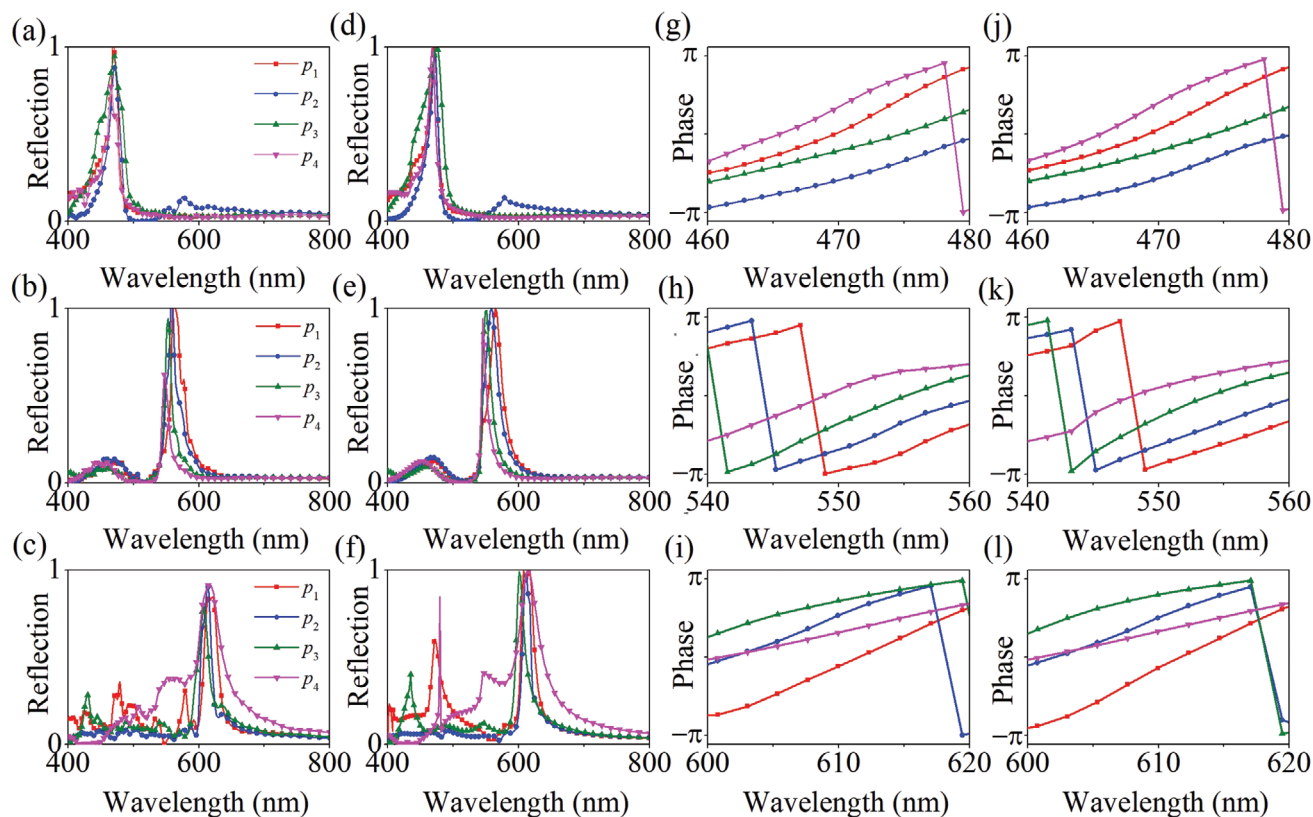


Figure 4. Panels (a) to (c) are predicted reflection spectra of the units designed by ES algorithm at three target wavelengths, respectively. Panels (d) to (f) are simulated reflection spectra of the units designed by ES algorithm at three target wavelengths. Panels (g) to (i) are the predicted phase curves of the units designed by ES algorithm at three target wavelengths. Panels (j) to (l) are the simulated phase curves of the units designed by ES algorithm at three target wavelengths. The structural parameters and phase values at the three target wavelengths can be found in Tables S3 and S4 (Supporting Information).

two-level phase distribution that can be treated as a two-level (0 and π) phase distribution with two additional phase options. The intensity of the conjugate image is suppressed compared with the pure two-level phase distribution. In order to avoid the influence of zero order light on the imaging plane, we use the off-axis design. The final image is designed to generate on the right side of zero order light. Figure 5b presents the top-view scanning electron microscope (SEM) images of the designed metasurface, which contains 240×240 pixels and each pixel is composed of at least 15×15 nanostructures. The multicolor holographic image was reconstructed and measured based on a home-built setup, as shown in Figure 5c. Three laser beams were combined together by a beam splitter BS1, and a pair of lenses (L1 and L2) was used to expand the laser beam. Polarizer (P1) was used to make the laser beam linear polarized, then the beam passed through the other beam splitter BS2, and illuminate on the metasurface. The reflected light of the sample was shunted to the other side by BS2, and the reconstructed image can be captured directly by a CCD camera at the focal plane of lens L3. Figure 5d–k shows the calculated and experimental reconstructed holographic images. There is a certain crosstalk between the wavelength channels of 470 and 610 nm in the calculated results. The image of flower designed at 610 nm can be observed at 470 nm. This crosstalk can be attributed to that the inversely designed nanostructures with operation wavelength

of 610 nm have nonzero reflection intensities at 470 nm, as shown in Figure 4c,f. Although the calculated results show a low crosstalk between different channels, the measured images of flowerpot and flower appear at 550 nm. Since the measured reflection spectra show certain differences compared with the simulated results in Figure 3, the crosstalk at 550 nm can be attributed to the size error of the fabricated sample. This results that the units corresponding to the blue part and red part still have high reflectivity at 550 nm. Meanwhile, additional background noises caused by the mutual coupling between different nanostructures at the boundaries of the pixels also lower the quality of the reconstructed holographic image. We can see the existence of conjugate images in both the calculated and experimental results, as we mentioned above, which is caused by the insufficient phase space value limited by the fewer structural configuration selection in the inverse design algorithm. The conjugate image can be further eliminated by increasing the modulated phase range via designing structures with complex shapes or relaxing the limitations on the nanostructures height and period. A detail discussion on the maximum phase and amplitude coverage of the nanostructures designed by the proposed inverse design method can be found in Figure S6 (Supporting Information). The experimental results further prove the effectiveness of our ES inverse design method. The designed metasurface can achieve high-efficient structural color

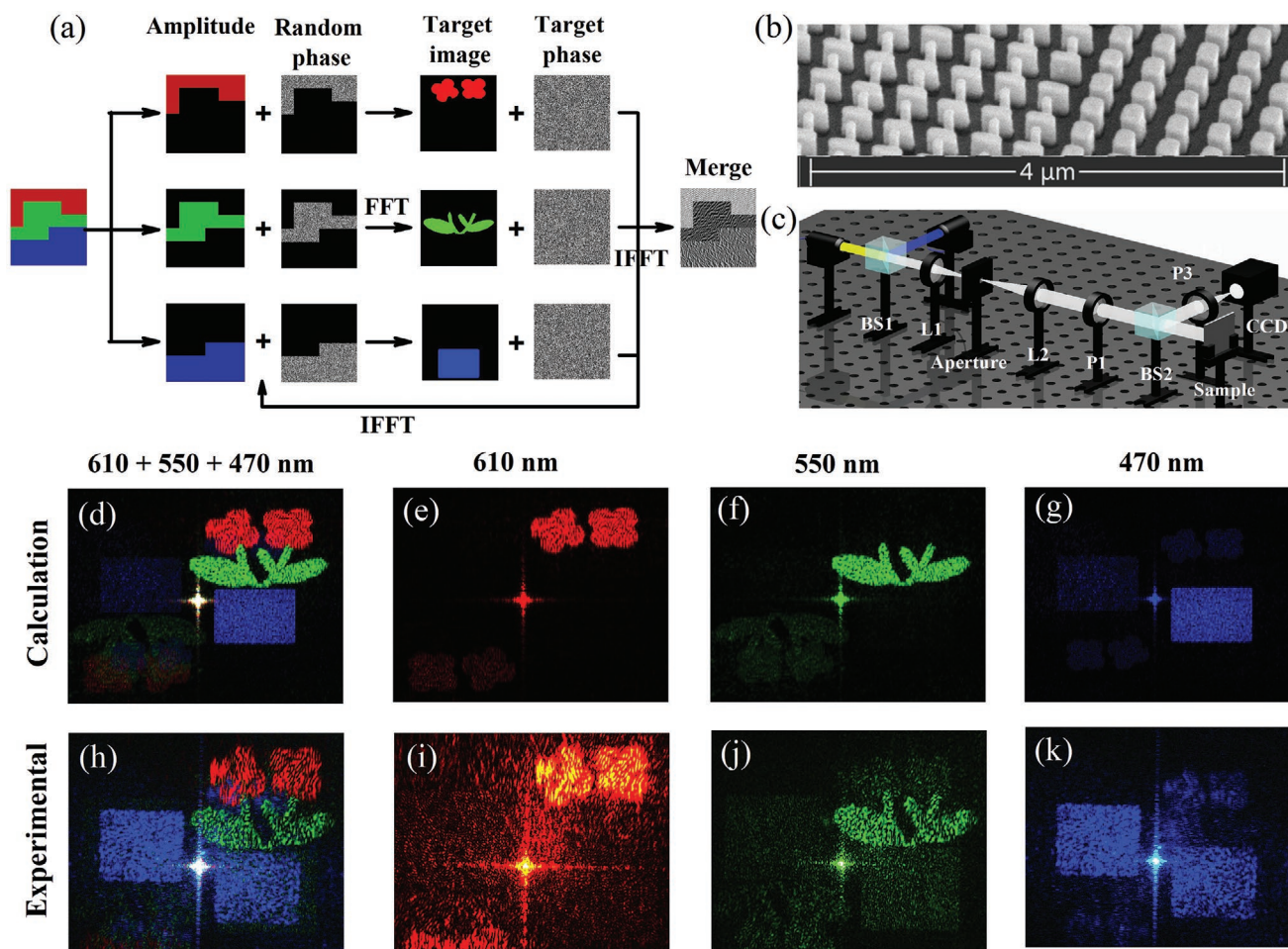


Figure 5. a) The flowchart of the GS algorithm to generate the phase profile. FFT is the fast Fourier transform and IFFT is the inverse fast Fourier transform. b) SEM image of the metasurface. c) Schematic illustrating the home-built setup to generate the holographic image. Using one beam splitter (BS1), three lasers beam (470, 550, and 610 nm) can be combined together. Two lenses (L1 and L2) are used to modify the spot of laser beam. The polarization of the laser can be changed into linear polarization by polarizer P1. And the beam splitter (BS2) can branch the reflected light of the samples to the other side, then the holographic image can be reconstructed at the focal plane of lens L3, which can be recorded directly by a CCD camera. Panels (d) to (g) are holographic reconstruction images obtained by calculation at different wavelengths. Panels (h) to (k) are experimental holographic reconstruction images obtained at different wavelengths.

under white light illumination, and it can generate color meta-holography under laser illumination.

3. Conclusion

In conclusion, we proposed an inverse design method based on DNN and ES algorithm to realize the inverse design of dielectric nanostructures with desired resonance wavelength, bandwidth, and phase delay. Compared with other inverse design method, the main advantage of the proposed method is that it does not need gradient information and can achieve multi-objective optimization. The combination of ES method and neural network also solves the problems of slow speed and large amount of computation in traditional ES algorithm. We have numerically and experimentally validated that the proposed method can be used to realize the inverse design of nanostructures

with on-demand structural colors and implement the multi-color meta-holography. The proposed inverse design method provides a promising candidate and can be widely used for the design of frequency multiplexing metasurface.

4. Experimental Section

Sample Fabrication: The proposed metasurface sample was fabricated on quartz wafer. A layer of positive electron beam resist (EBR) with a thickness of 300 nm was spin-coated on the substrate. Then, a thin conductive polymer Espacer was spin-coated to avoid charging effects during electron-beam writing. Next, the structure patterns were exposed by an electron beam lithography (EBL) system (JEOL 6300FS) at 100 kV. After EBL, the Espacer was rinsed with deionized water and sample was developed in MIBK:IPA = 1:3 for 3 min under gentle agitation. The TiO₂ was deposited onto the exposed EBR through atomic layer deposition. And a blanket film of TiO₂ was removed with reactive ion etching using a mixture of Cl₂, BCl₃, and Ar gas. After the resist was removed by PG remover, the TiO₂ sample was created.

Numerical Simulation: The required data over the operating spectrum were calculated using the numerical simulation package CST Microwave Studio, with the unit cell boundary condition applied for all nanostructures in both x and y directions and open boundaries implemented in both the negative and positive z -directions. In all the simulations, the refractive index of SiO_2 substrate was set at 1.5, and the extinction coefficients of it can be negligible. The optical parameters of TiO_2 are taken from ref. [42]. The center of the nanorod was located at (0,0), and the centers of the two structures in the dimer were located at $(-\frac{1}{4}p_x, 0)$ and $(\frac{1}{4}p_x, 0)$ respectively. The value ranges of nanorod parameters were (unit: nm): $p_x \in [250, 400]$, $p_y \in [250, 400]$, $h \in [150, 400]$, $l \in [50, p_x-50]$, $w \in [50, p_y-50]$. The value ranges of dimer parameters were: $p_x \in [280, 500]$, $p_y \in [280, 500]$, $h \in [250, 500]$, $l_1 \in [35, \frac{1}{4}p_x-35]$, $l_2 \in [35, \frac{1}{4}p_x-35]$, $l_3 \in [35, \frac{1}{4}p_x-35]$, $l_4 \in [35, \frac{1}{4}p_x-35]$, $w_1 \in [70, p_y-70]$, $w_2 \in [70, p_y-70]$.

Supporting Information

Supporting Information is available from the Wiley Online Library or from the author.

Acknowledgements

D.M. and Z.L. contributed equally to this work. This work was supported by the National Key Research and Development Program of China (Grants No. 2021YFA1400601 and 2017YFA0303800), the National Natural Science Fund for Distinguished Young Scholar (Grant No. 11925403), the National Natural Science Foundation of China (Grants No. 12122406, 12192253, 11974193, 11904181, and 11904183), the Natural Science Foundation of Tianjin for Distinguished Young Scientists (Grant No. 18JCQJC45700), and the China Postdoctoral Science Foundation (2018M640224 and 2021M690084).

Conflict of Interest

The authors declare no conflict of interest.

Data Availability Statement

The data that support the findings of this study are available from the corresponding author upon reasonable request.

Keywords

evolution strategy, inverse design, meta-holography, multicolor, neural networks

Received: December 3, 2021

Revised: March 19, 2022

Published online:

[1] K. Koshelev, Y. Kivshar, *ACS Photonics* **2020**, *8*, 102.

[2] X. Luo, *Adv. Mater.* **2019**, *31*, 1804680.

[3] W. T. Chen, F. Capasso, *Appl. Phys. Lett.* **2021**, *118*, 100503.

[4] S. Sun, Q. He, J. Hao, S. Xiao, L. Zhou, *Adv. Opt. Photonics* **2019**, *11*, 380.

- [5] S. Chen, Z. Li, W. Liu, H. Cheng, J. Tian, *Adv. Mater.* **2019**, *31*, 1802458.
- [6] H. H. Hsiao, C. H. Chu, D. P. Tsai, *Small Methods* **2017**, *1*, 1600064.
- [7] X. Ni, Z. J. Wong, M. Mrejen, Y. Wang, X. Zhang, *Science* **2015**, *349*, 1310.
- [8] Y. Yang, L. Jing, B. Zheng, R. Hao, W. Yin, E. Li, C. M. Soukoulis, H. Chen, *Adv. Mater.* **2016**, *28*, 6866.
- [9] R. C. Devlin, A. Ambrosio, N. A. Rubin, J. B. Mueller, F. Capasso, *Science* **2017**, *358*, 896.
- [10] J. Jin, M. Pu, Y. Wang, X. Li, X. Ma, J. Luo, Z. Zhao, P. Gao, X. Luo, *Adv. Mater. Tech.* **2017**, *2*, 1600201.
- [11] Q. Wang, E. Plum, Q. Yang, X. Zhang, Q. Xu, Y. Xu, J. Han, W. Zhang, *Light: Sci. Appl.* **2018**, *7*, 25.
- [12] G. Yoon, D. Lee, K. T. Nam, J. Rho, *ACS Photonics* **2017**, *5*, 1643.
- [13] W. Liu, Z. Li, H. Cheng, C. Tang, J. Li, S. Zhang, S. Chen, J. Tian, *Adv. Mater.* **2018**, *30*, 1706368.
- [14] M. Khorasaninejad, W. T. Chen, R. C. Devlin, J. Oh, A. Y. Zhu, F. Capasso, *Science* **2016**, *352*, 1190.
- [15] X. Ni, A. V. Kildishev, V. M. Shalae, *Nat. Commun.* **2013**, *4*, 2807.
- [16] Y. Yifat, M. Eitan, Z. Iluz, Y. Hanein, A. Boag, J. Scheuer, *Nano Lett.* **2014**, *14*, 2485.
- [17] Q. Wei, L. Huang, X. Li, J. Liu, Y. Wang, *Adv. Opt. Mater.* **2017**, *5*, 1700434.
- [18] Q. Wang, X. Zhang, E. Plum, Q. Xu, M. Wei, Y. Xu, H. Zhang, Y. Liao, J. Gu, J. Han, W. Zhang, *Adv. Opt. Mater.* **2017**, *5*, 1700277.
- [19] Y. Gao, Y. Fan, Y. Wang, W. Yang, Q. Song, S. Xiao, *Nano Lett.* **2018**, *18*, 8054.
- [20] G. Qu, W. Yang, Q. Song, Y. Liu, C. W. Qiu, J. Han, D.-P. Tsai, S. Xiao, *Nat. Commun.* **2020**, *11*, 5484.
- [21] G. Zheng, H. Mühlenbernd, M. Kenney, G. Li, T. Zentgraf, S. Zhang, *Nat. Nanotech.* **2015**, *10*, 308.
- [22] L. Wang, S. Kruk, H. Tang, T. Li, I. Kravchenko, D. N. Neshev, Y. S. Kivshar, *Optica* **2016**, *3*, 1504.
- [23] A. Martins, J. Li, A. F. da Mota, Y. Wang, L. G. Neto, J. P. do Carmo, F. L. Teixeira, E. R. Martins, B. H. V. Borges, *Opt. Express* **2018**, *26*, 9573.
- [24] W. Wan, J. Gao, X. Yang, *ACS Nano* **2016**, *10*, 10671.
- [25] X. Li, L. Chen, Y. Li, X. Zhang, M. Pu, Z. Zhao, X. Ma, Y. Wang, M. Hong, X. Luo, *Sci. Adv.* **2016**, *2*, e1601102.
- [26] X. Zhang, M. Pu, Y. Guo, J. Jin, X. Li, X. Ma, J. Luo, C. Wang, X. Luo, *Adv. Funct. Mater.* **2019**, *29*, 1809145.
- [27] Y. Hu, L. Li, Y. Wang, M. Meng, L. Jin, X. Luo, Y. Chen, X. Li, S. Xiao, H. Wang, Y. Luo, C.-W. Qiu, H. Duan, *Nano Lett.* **2019**, *20*, 994.
- [28] Y. W. Huang, W. T. Chen, W. Y. Tsai, P. C. Wu, C. M. Wang, G. Sun, D. P. Tsai, *Nano Lett.* **2015**, *15*, 3122.
- [29] W. Zhao, B. Liu, H. Jiang, J. Song, Y. Pei, Y. Jiang, *Opt. Lett.* **2016**, *41*, 147.
- [30] B. Wang, F. Dong, Q. T. Li, D. Yang, C. Sun, J. Chen, Z. Song, L. Xu, W. Chu, Y.-F. Xiao, Q. Gong, Y. Li, *Nano Lett.* **2016**, *16*, 5235.
- [31] Y. Hu, X. Luo, Y. Chen, Q. Liu, X. Li, Y. Wang, N. Liu, H. Duan, *Light: Sci. Appl.* **2019**, *8*, 86.
- [32] B. Wang, F. Dong, D. Yang, Z. Song, L. Xu, W. Chu, Q. Gong, Y. Li, *Optica* **2017**, *4*, 1368.
- [33] W. Ma, Z. Liu, Z. A. Kudyshev, A. Boltasseva, W. Cai, Y. Liu, *Nat. Photon.* **2021**, *15*, 77.
- [34] L. Meier, P. Tanskanen, L. Heng, G. H. Lee, F. Fraundorfer, M. Pollefeys, *Autonomous Robots* **2012**, *33*, 21.
- [35] G. Hinton, L. Deng, D. Yu, G. E. Dahl, A. R. Mohamed, N. Jaitly, A. Senior, V. Vanhoucke, P. Nguyen, T. N. Sainath, B. Kingsbury, *IEEE Signal processing magazine* **2012**, *29*, 82.
- [36] J. Vassileva, S. Breban, M. Horsch, *Computational Intelligence* **2002**, *18*, 583.
- [37] W. Ma, F. Cheng, Y. Liu, *ACS Nano* **2018**, *12*, 6326.

- [38] L. Gao, X. Li, D. Liu, L. Wang, Z. Yu, *Adv. Mater.* **2019**, *31*, 1905467.
- [39] S. An, C. Fowler, B. Zheng, M. Y. Shalaginov, H. Tang, H. Li, L. Zhou, J. Ding, A. N. Agarwal, C. Rivero-Baleine, K. A. Richardson, T. Gu, J. Hu, H. Zhang, *ACS Photonics* **2019**, *6*, 3196.
- [40] Z. Liu, D. Zhu, S. P. Rodrigues, K. T. Lee, W. Cai, *Nano Lett.* **2018**, *18*, 6570.
- [41] W. Liu, D. Ma, Z. Li, H. Cheng, D. Y. Choi, J. Tian, S. Chen, *Optica* **2020**, *7*, 406039.
- [42] B. Yang, W. Liu, Z. Li, H. Cheng, D. K. Choi, S. Chen, J. Tian, *Nano Lett.* **2019**, *19*, 4221.